AIAA JOURNAL
Vol. 46, No. 1, January 2008

Delayed Detached-Eddy Simulation and Analysis of Supersonic Inlet Buzz

S. Trapier,* S. Deck,† and P. Duveau†
ONERA, 92322 Châtillon, France

DOI: 10.2514/1.32187

Supersonic inlet buzz in a rectangular, mixed-compression inlet has been simulated on a 20 × 10^6 points mesh using the delayed detached-eddy simulation method, a version of detached-eddy simulation that ensures the attached boundary layers are treated using Reynolds-averaged Navier–Stokes equations. The results are compared with experimental data obtained during a previous campaign of wind-tunnel experiments. The comparison of unsteady data is performed thanks to phase averages, Fourier transforms, and wavelet transforms. The buzz observed at Mach 1.8, which occurred at a frequency of 18 Hz, is well reproduced. The shock oscillations, as well as the different flow features experimentally observed, are present in the simulation. The buzz frequency, as well as higher frequencies existing in the experimental pressure signals, are correctly predicted. The data issued from the simulation (time history of pressure fluctuations, pseudo-Schlieren, and three-dimensional visualizations) allow a better investigation of the inlet flowfield during buzz and a detailed description and physical analysis of this phenomenon. A description and an explanation of the mechanism at the origin of secondary oscillations that occur at a higher frequency during buzz are proposed. The crucial role of acoustic waves moving through the duct is shown.

Nomenclature

A_c = inlet capture area, m^2
C_{DES} = constant of detached-eddy simulation, dimensionless
c = speed of sound, m/s
d = distance to closest wall, m
$\tilde{d}_{\mathrm{DES97}}$ = length scale of DES97, m
$\tilde{d}$ = length scale of delayed detached-eddy simulation, m
f = frequency, Hz
f_d = function of delayed detached-eddy simulation, dimensionless
h = inlet height, m
M = Mach number, dimensionless
p = pressure, Pa
t = time, s
u = streamwise flow velocity, m/s
$W_x(t, f)$ = wavelet transform of signal $x(t)$; if $x(t)$ is in pascal, $|W_x(t, f)|^2$, $WV_x(t, f)$ is in Pa$^2 \cdot$ s$^{-1} \cdot$ Hz^{-1}
x, y, z = coordinates, m
x^+, y^+, z^+ = coordinates in wall units, dimensionless
$\Delta_x, \Delta_y, \Delta_z$ = cell sizes in local coordinate system, m
Δ = maximum cell size = $\max(\Delta_x, \Delta_y, \Delta_z)$, m
$\tilde{\nu}$ = pseudoeddy viscosity, m$^2 \cdot$ s^{-1}
ν_t = eddy viscosity, m$^2 \cdot$ s^{-1}
ν = molecular viscosity, m$^2 \cdot$ s^{-1}

I. Introduction

INLET buzz is a phenomenon of self-sustained shock oscillations that may appear in almost every type of supersonic inlets, and which results in high-amplitude variations of the inlet mass flow and pressure. It generally arises when the entering mass flow is reduced below a given value, the so-called buzz limit. Inlet buzz can lead to thrust loss, engine surge, or even cause structural damages to the aircraft; this violent and dangerous phenomenon is therefore highly undesirable. Buzz holds an important place in the conception of an inlet, and more generally of the propulsion of a supersonic aircraft, because it imposes the lower limit of air mass flow passing through the engine. The ability to know with precision the buzz limit of an inlet is therefore important; otherwise, one would have to take very large security margins when operating the engine to avoid buzz and, consequently, needlessly restrict the possibilities of the engine. Today, the only way to get an accurate knowledge of the buzz limit of an inlet is a long and costly campaign of wind-tunnel tests. It would be of great interest to have a reliable numerical method capable of precisely predicting the buzz limit.

Inlet buzz was first observed and described by Oswatitsch [1] in 1944. Experimental [2–7], analytical [8–10], and numerical [11–13] studies have been carried out since, to get a better understanding of this phenomenon and to avoid or delay its onset.

On the experimental and theoretical side, some progress has been made in the understanding of the physical mechanisms that trigger the instability. It is now well established that buzz is triggered by a shear layer, issued from the intersection point of normal and oblique shocks, entering the cowl lip [2] (Ferri criterion), and/or a shock-induced separation developing on the compression surface, which obstructs the inlet [3] (Dailey criterion). Theoretical models of the phenomenon have been developed [8,9], but this kind of linear analyses, based on highly idealized models and fluid flows, fail to give a precise representation of this complex phenomenon. Although several approximate methods have been proposed, it is today still impossible to precisely predict the onset of inlet buzz.

We presented in [14] the first results of an experimental study that was conducted in ONERA supersonic wind tunnel S3MA on a rectangular, mixed-compression inlet model. The purpose was to build a database and to improve the knowledge of buzz. Two kinds of shock oscillations were observed. They were called “little buzz” and “big buzz”, following Fisher et al. [5], and they occurred at frequencies, respectively, around 120 and 18 Hz. Little buzz is thought to be due to an acoustic resonance phenomenon excited by the presence of a shear layer under the cowl lip, whereas big buzz seems to be triggered by a boundary-layer separation on the compression ramps. Signal processing analyses of unsteady pressure recordings showed that the big buzz frequency was already present in the flow before the onset of large-amplitude shock oscillations, which suggested that the underlying mechanism of big buzz,

---

Received 16 May 2007; revision received 2 July 2007; accepted for publication 3 July 2007.

*Ph.D. Student, Applied Aerodynamics Department.

†Research Scientist, Applied Aerodynamics Department.

probably linked to acoustics, already exists before buzz starts [14]. A detailed analysis of the experimental data obtained at Mach numbers 1.8 and 2 has been carried on using advanced signal processing tools such as wavelet transform. It is presented in [15], as well as a method to predict buzz onset online thanks to change detection algorithms.

On the numerical side, to the author's knowledge, Newsome [11] conducted the first Navier–Stokes computations. Other attempts to simulate buzz thanks to Euler or Reynolds-averaged Navier–Stokes (RANS) simulations have been made, by Lu and Jain [12] and Fujiwara et al. [13] for instance. They proved that a numerical model as simple as Euler manages to reproduce qualitatively the phenomenon. However, several experimental studies [3,5,16] have shown the crucial role of flow features such as shock-boundary layer interaction, massively separated areas, and three-dimensional flows in the occurrence of buzz. Classical Euler or RANS numerical methods could therefore be insufficient to provide an accurate, quantitative simulation of buzz, and the use of advanced methods such as hybrid RANS/LES (large-eddy simulation) approaches could turn out to be necessary.

In the present study, the buzz at Mach 1.8 was simulated thanks to the detached-eddy simulation (DES) method. This method often meets the problem of "modeled stress depletion," which occurs when boundary layers are treated in LES mode. To address this problem, we used here the delayed DES (DDES) approach, which is designed to automatically detect attached boundary layers and ensures they are treated in RANS mode [16]. This method is particularly adapted to the simulation of buzz, because this phenomenon implies large-amplitude motion of separated regions whose location is not fixed by the geometry.

The objective of the current study is threefold: 1) to assess the capability of DDES to simulate big buzz, 2) to compare numerical results with the available experimental data, and 3) to investigate the unsteady aerodynamic field not accessible by the experiment to get a better knowledge of buzz flow and of the physical causes of the phenomenon.

II. Experimental Data

Experiments were conducted in ONERA supersonic wind-tunnel S3MA (Modane, France) on a rectangular, mixed-compression inlet model (Fig. 1). The design Mach number, i.e., the Mach number in which the ramp shocks hit the lip, is two. The external compression, which represents 85% of the total compression, is achieved by three ramps inclined by 5.5, 11.18, and 17.11 deg to the freestream flow direction. The internal compression (15% of the total compression) is achieved by a convergent. The vertical height of the cowl lip above the ramp tip is 100 mm, and the inlet width is constant equal to 100 mm. The inlet capture area is $A_c = 0.01\ \mathrm{m}^2$. The diffuser length is 535 mm. Its final section is square ($100 \times 100\ \mathrm{mm}^2$).

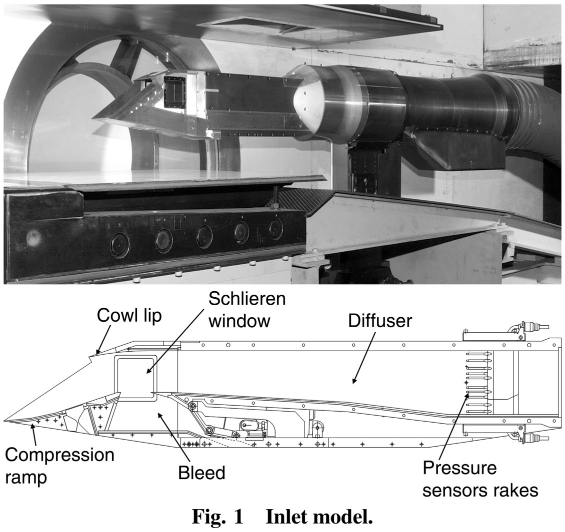

Fig. 1 Inlet model.

To control the entering mass flow, the exit section of the duct is a sonic throat, which can be throttled by a butterfly valve. The total length of the duct, between the cowl lip and the exit sonic throat, is 1861 mm.

Sidewall windows allow one to view the flow and the shocks inside the inlet thanks to Schlieren pictures and videos (500 frames/s). The model is equipped with a lot of pressure sensors: on the upstream part of the model, 30.

Kulite sensors measured the unsteady static pressures on the compression ramps, on one sidewall, and under the cowl lip. At the diffuser end, four rakes with five total pressure sensors each, six static pressure sensors, and two Kulites allow estimating of the pressure recovery of the inlet. The mass flow is measured by a sonic throat mass flow meter.

The model can be equipped or not with a boundary-layer bleed in the vicinity of the inlet throat.

Only the main results at Mach 1.8 are presented here, focusing on the results without bleed. A more detailed description of the experimental study can be found in [14].

At this Mach number, the Reynolds number based on the inlet height (0.1 m) is 2.9×10^6. The flow regime before buzz is subcritical, i.e., there is an external shock located on the compression ramps, and the flow entering the inlet is subsonic.

When the mass flow decreases, the shock moves upstream along the ramps until buzz begins. Buzz start is thought to be triggered by a separation at the foot of the normal shock, on the compression ramps [14]. The shock then begins to oscillate; it moves upstream to the ramp tip (and a separated zone develops on the ramps), then moves back downstream, and an internal shock appears inside the inlet (at this time, the situation is similar to the supercritical regime, although the throttling has not changed). This internal shock moves back and forth inside the duct, travels back upstream, and disappears when merging with the external shock. These shock motions are cyclic and periodical, at a characteristic frequency around 18 Hz.

Sketches on Fig. 2 describe these shock motions. Fig. 3 shows the corresponding Schlieren pictures taken during a buzz cycle, on which they can be seen.

Figure 4 shows the pressure signals recorded by several sensors located, respectively, on the ramp tip (K18), under the cowl lip (K14), and in the diffuser (PS33) during buzz. A buzz cycle clearly appears on these records; the subcritical and supercritical phases can be seen. During the subcritical phase, sensor K18 is located in a supersonic area (low and constant pressure), whereas the sensors located inside the inlet are in a subsonic region. During the supercritical phase, the flow under the cowl lip is supersonic (sensor K14). Secondary oscillations that occur at a frequency around

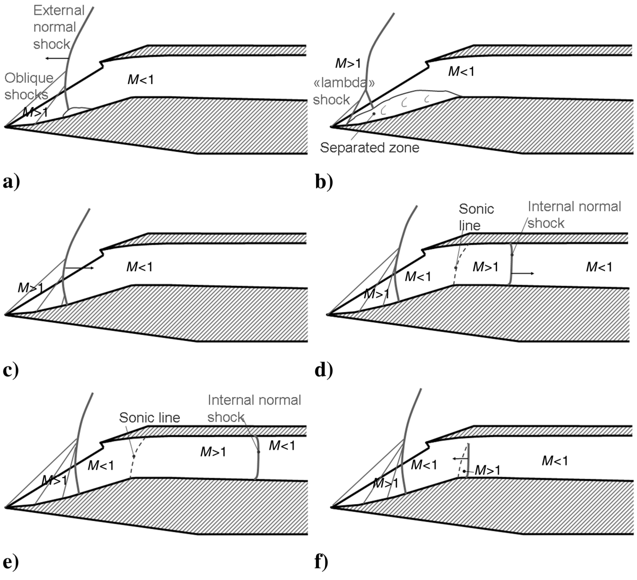

Fig. 2 Shock motions during a buzz cycle.

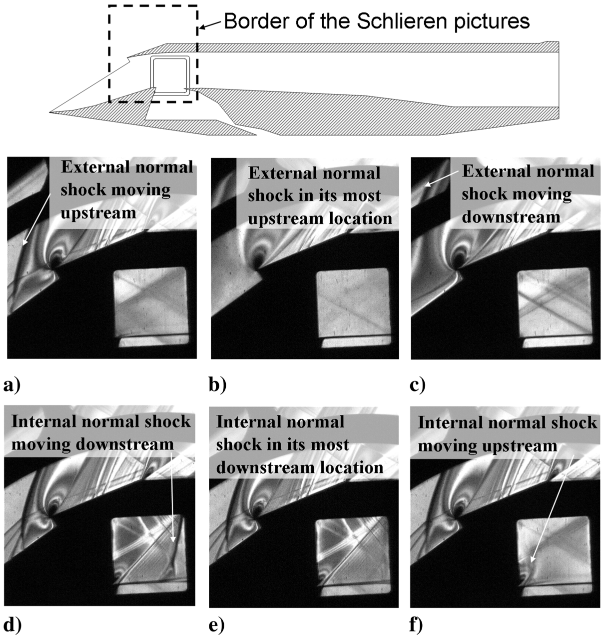

Fig. 3 Schlieren pictures taken during a buzz cycle.

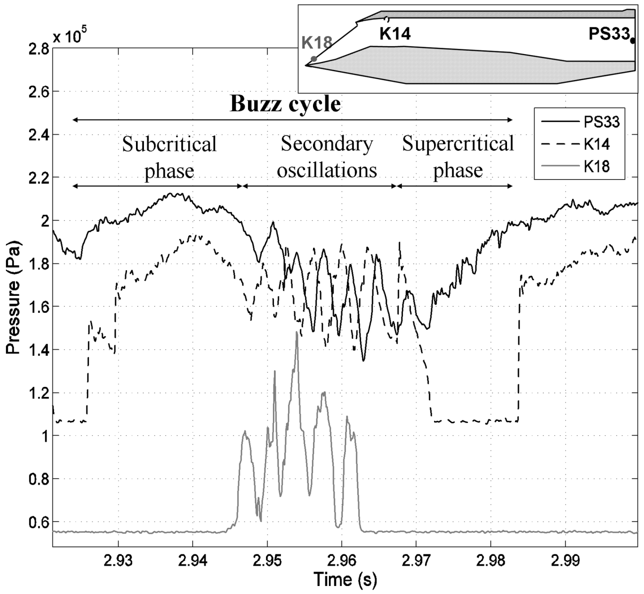

Fig. 4 Pressure records during big buzz ($M = 1.8$).

200 Hz can be seen when the normal shock is at its most upstream location, on the ramp tip. These oscillations were already observed by Dailey [3]. Their mechanism will be detailed in a subsequent section.

III. Numerical Method

A. General Description

All computations presented in the present paper have been conducted using the FLU3M solver, developed by ONERA. This code solves the Navier–Stokes equations on multiblock structured grids. The computational domain is divided by blocks, composed of hexahedral cells. The time integration is carried out by means of the second-order-accurate backward scheme of Gear. Roe's flux-difference splitting is employed for the advective fluxes, MUSCL approach extends the spatial accuracy to the third order (third-order upwind biased), and is combined with Jameson's sensor to satisfy total variation diminishing (TVD) conditions on shocks. Further details concerning the numerical method and implementation of turbulence models can be found in [17,18].

This numerical strategy has already been used to perform large-eddy simulation of the flow around a low-pressure turbine blade [19], as well as over a cavity at high Reynolds number [20]. It has also been successfully used to compute zonal detached-eddy simulation (ZDES) of transonic buffet over a supercritical airfoil [21] and of an unsteady axisymmetric separating–reattaching flow [22], to perform direct numerical simulation (DNS) and LES of active separation control by a synthetic jet [23], and to compute hybrid RANS/LES of a supersonic base flow [24].

B. Delayed Detached-Eddy Simulation

Detached-eddy simulation is a hybrid RANS/LES approach that was originally proposed by Spalart et al. in 1997 [25]. Their motivation was to combine the best features of a RANS approach with the best features of LES; the RANS approach predicts the attached flows quite well with a low computational cost, whereas LES has a high-computational cost but can predict the separated flows more accurately. DES was designed to treat the boundary layers using a RANS model and to apply an LES treatment to separated regions.

The original DES model (named DES97 in the following) was based on the Spalart–Allmaras (SA) RANS model which solves a one-equation turbulence model for the eddy viscosity $\tilde{\nu}$. This model is provided with a destruction term for the eddy viscosity that contains d, the distance to the closest wall. This term, when balanced with the production term, adjusts the eddy viscosity to scale with local deformation rate $\tilde{S}$ producing an eddy viscosity given by

$$\tilde{\nu} \approx \tilde{S} d^2 \tag{1}$$

The idea suggested by Spalart et al. [25] was to modify the destruction term so that the RANS model is reduced to an LES subgrid-scale one in the detached flows. They proposed to replace d with a new length, $\tilde{d}_{\mathrm{DES97}}$:

$$\tilde{d}_{\mathrm{DES97}} = \min(d, C_{\mathrm{DES}}\Delta) \tag{2}$$

where C_{DES} is a constant equal to 0.65 and $\Delta = \max(\Delta_x, \Delta_y, \Delta_z)$ is the cell characteristic size. The use of the maximum cell size for Δ is physically justified as it controls which wavelengths can be resolved and the eddy-viscosity level. In the attached boundary layer, due to the grid anisotropy ($\Delta_x, \approx \Delta_z \gg \Delta_y$) typical of this flow region, in accordance with Eq. (2), $\tilde{d}_{\mathrm{DES97}} = d$, and the model reduces to the standard SA RANS model. Otherwise, once a field point is far enough from walls ($d > C_{\mathrm{DES}}\Delta$), the length scale of the model performs as a subgrid-scale version of the SA model.

A major issue in the use of this approach is the existence of a "gray area" between the RANS and LES regions, whose location depends on grid spacing. In the natural use of DES, the grid spacing should make this area be located outside of the boundary layers, which will then be treated in RANS. With a very fine grid, on the other hand, the LES mode of DES will be activated everywhere in the flow, including boundary layers, which is nothing to worry about because the grid is fine enough to support LES treatment of the boundary layer.

Problems arise in the intermediate case: ambiguous grids can lead the gray area to be located inside the boundary layer, where these grids are not fine enough to support resolved velocity fluctuations, i.e., "LES content." This causes, in the part of the boundary layer that is unfortunately treated in LES mode, a drop in the eddy viscosity and therefore in the modeled Reynold stress without any sizeable resolved stress to restore the balance. This phenomenon is referred to as modeled stress depletion (MSD). The depleted stresses decrease the skin-friction coefficient and this can possibly result in premature boundary layer separation or "grid-induced separation" (GIS), as described in [26] (see also discussion in [27], pp. 267–275).

To avoid this, a solution can be zonal DES, in which RANS mode is explicitly imposed in selected regions, where an attached boundary layer is expected [21,28]. However, in the case of inlet buzz, separated areas move with large amplitude so that the selected regions would be totally different from one phase of a buzz cycle to the other. This method cannot therefore be used here.

A more adapted solution to the present case is delayed detached-eddy simulation [16]. This method is designed to "shield" the boundary layer, i.e., to automatically preserve RANS mode inside it. It has been successfully tested on different flows: in a boundary layer, on a single and multi-element airfoil, a cylinder, and a backward-facing step [16]. These tests demonstrated that RANS function is maintained in thick boundary layers, without preventing LES function after massive separation.

The formulation of DDES uses the quantity

$$r_d = \frac{\nu_t + \nu}{\sqrt{U_{i,j}U_{i,j}}\kappa^2 d^2} \tag{3}$$

where ν_t is the kinematic eddy viscosity, ν is the molecular kinematic viscosity, $U_{i,j}$ is the velocity gradients, κ is the Karman constant, and d is the distance to the wall. This parameter r_d is equal to one in a logarithmic layer, and falls to zero at the edge of the boundary layer. It is used in the function

$$f_d = 1 - \tanh[(8r_d)^3] \tag{4}$$

which is equal to zero in the boundary layer and one elsewhere.

Whereas in DES97, the length scale is as in Eq. (2), in DDES, this length scale is redefined:

$$\tilde{d} = d - f_d \max(0, d - C_{\mathrm{DES}}\Delta) \tag{5}$$

In the boundary layers ($f_d = 0$), $\tilde{d}$ is equal to d (like in RANS), and elsewhere ($f_d = 1$), $\tilde{d}$ is like in DES97. This ensures that boundary layers are fully treated in RANS mode.

C. Grid

As well as in LES, the grid generation in DES is a key issue, because the grid spacing controls which wavelengths can be resolved, as well as the eddy-viscosity levels. In the present case, we have to simulate an internal flow featuring four boundary layers (on the lower, upper, and side walls). Each one of these boundary layers has to be finely meshed.

The grid is divided into 48 blocks. Its geometry is shown in Fig. 5. Twenty-two blocks are used to mesh the internal flow (i.e., the streamtube entering the inlet), and 26 to mesh the external flow, which allowed us to apply the far-field conditions. The mesh is particularly refined over the compression ramps and in the inlet section, which are the crucial zones for buzz; around half of the points are located there. A zoom on the mesh at the walls in this area can be seen in Fig. 5.

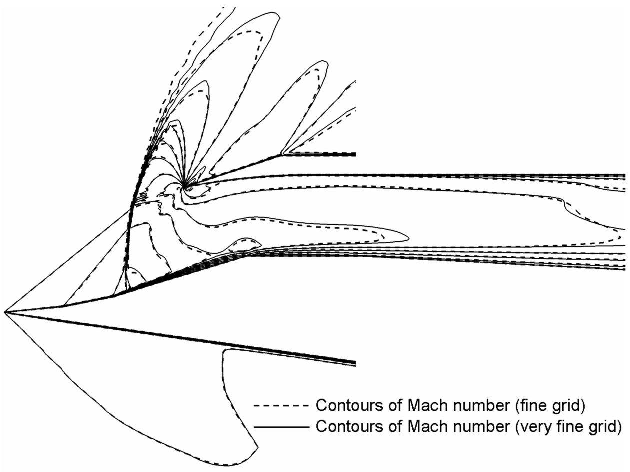

Fig. 6 Contours of Mach number on fine grid (10 x 10^6 points) and very fine grid (20 x 10^6 points).

The whole length of the duct and the exit section are meshed (the butterfly valve is replaced in the simulation by a sonic throat with a circular section). This part of the grid exists to comply with the acoustic lengths of the model, but the mesh in this area is much coarser, in particular in the streamwise direction.

Grid convergence for hybrid RANS/LES simulations is a complex issue. Indeed, in LES mode there is no possible grid convergence in a RANS sense, because the mesh size impacts the ratio between modeled and resolved turbulence; which is why we checked grid convergence in RANS.

A RANS computation was performed on two grids containing, respectively, 10 million and 20 million points, both with the same exit throat section for which the inlet flow is subcritical and stable. The Mach number contours in the symmetry plane of the inlet obtained for both grids are compared in Fig. 6. The differences between the results yielded from the two grids are small, and the location of the normal shock on the compression ramp, in particular, is the same. The grid convergence in RANS is therefore achieved.

The grid that was used for DDES calculations, and which is described in the following, is the very fine grid (20 million points). This grid was designed to fulfill DES requirements. The mesh of the symmetry plane of the inlet and of the lower wall for this latter grid is plotted in Fig. 7 (every other point is shown in each direction).

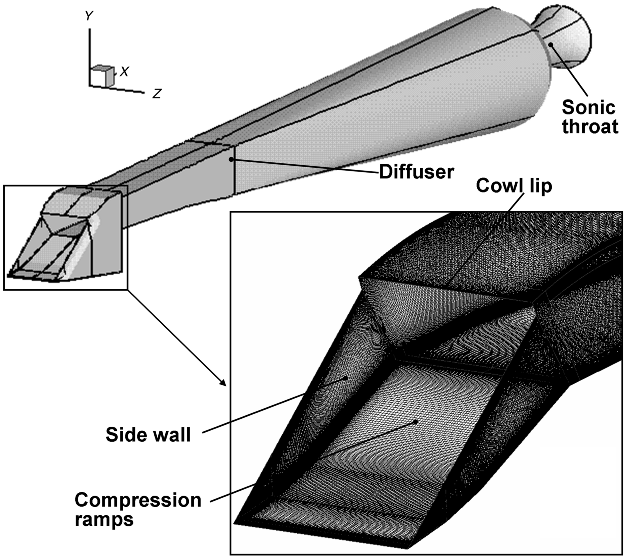

Fig. 5 Geometry of the grid.

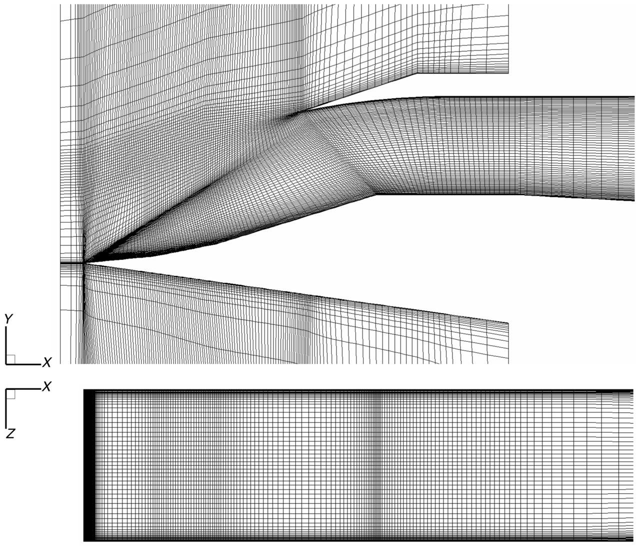

Fig. 7 Mesh of the symmetry plane of the inlet (top) and of the lower wall (bottom) for the very fine grid. Every other point is shown.

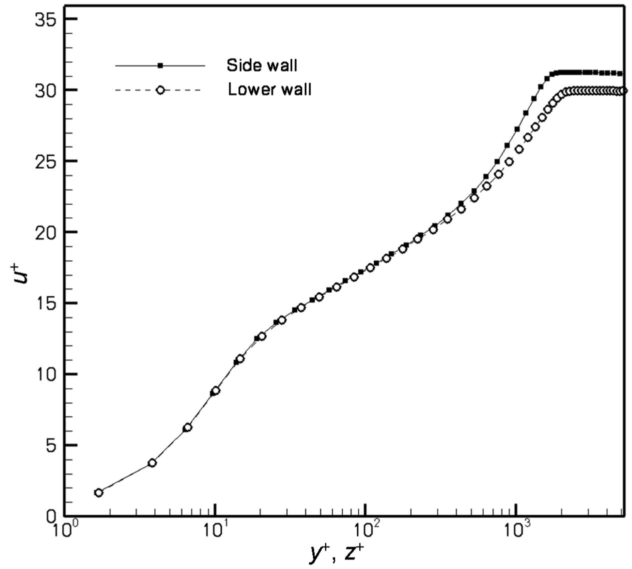

Fig. 8 Profile of boundary layers in wall units on the side and lower walls, for the very fine grid.

The captured streamtube (whose dimensions are 0.1 m × 0.1 m) is meshed using 174 cells in the vertical direction and 152 cells in the spanwise direction. In both directions, 60 of these cells are located in the boundary layers. Figure 8 shows the velocity profiles in the boundary layers, in wall units, on the lower wall (compression ramps), and on the side wall. On the compression ramps as well as on both sidewalls, the boundary layer contains around 30 points (the values of y^+ and z^+, respectively, are at worst between one and two at the first point off the wall). Over the compression ramps, the grid extensions in the streamwise direction Δx and in the spanwise direction Δz were chosen to have $\Delta x \approx \Delta z$, following Spalart's recommendations for DES grids [29]. The highest values of these grid extensions are 1 mm (x^+ and z^+ are composed of between 50 in the vicinity of the ramp tip to, at worst, 600 in the center of the third ramp).

D. Computational Description

A global time step is used for all computations. The time step for unsteady calculations is 5 μs, which results in Courant–Friedrich–Levy (CFL) numbers based on maximum acoustic velocity $u + c$ (where c denotes the local speed of sound) comprising between 1 and 5 in the flow and at most 15 in the boundary layers (even if much higher values are reached, very locally, in the smallest cells around the ramp tip). All unsteady simulations have been performed with five Newton inner iterations (see Péchier et al. [17] for further details), and the temporal accuracy was checked during the convergence process of the inner iterations (a drop of the residue values of at least one order is reached).

The CPU cost per cell and per inner iteration is around 0.5 μs. The simulations were performed on two processors of a NEC-SX8 computer. To make possible an accurate signal processing analysis, ten buzz cycles were simulated. The total CPU cost of the calculation was approximately 1600 h.

Unsteady RANS calculations were also performed on the 20 million point grid, for comparison with DDES results (as shown later).

The procedure that is used to trigger buzz is the following: the simulation is initialized with a flow given by a steady RANS calculation, with an exit sonic throat section large enough to ensure that the external shock is stable. Then the throat section is reduced at the beginning of the unsteady DDES simulation. This reduction generates a compression wave that travels upstream in the duct. When this wave finally meets the external shock, buzz starts after a transient phase of shock displacement. The real unsteady calculation begins and the time-averaging process is turned on. The statistics were collected during six buzz cycles.

E. Behavior of DDES

Figure 9a shows the contour of velocity u in the upstream part of the inlet, during the phase of buzz where the flow on the ramps is attached. The corresponding contour of function f_d is also shown. On the right of the figure are plotted different variables and functions used by the DDES. Figure 9b shows the equivalent contours and plots during the phase where the flow is separated.

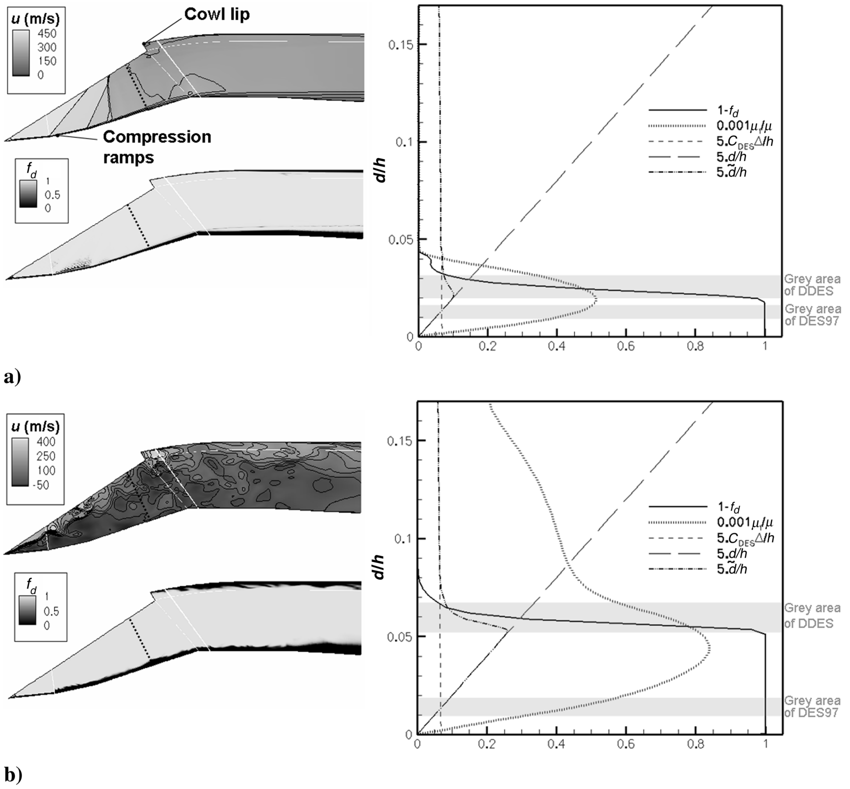

Fig. 9 DDES behavior when the flow is a) attached and b) separated. Inlet height h is 0.1 m, μ_t is the eddy viscosity, and μ is the molecular viscosity.

One can check that in both cases the function f_d is zero in the boundary layers (and so $\tilde{d}$ is equal to d, the RANS mode is preserved) and one elsewhere (and so $\tilde{d} = C_{\mathrm{DES}}\Delta$, the LES mode is used). The function f_d shows to be robust, because it behaves adequately for both flows (one is attached and the other is fully separated).

On the plots on the right it can be noticed that the maximum of μ_t/μ is reached inside the RANS zone (i.e., where $f_d = 0$), which means that the boundary layer is correctly "shielded." In the separated case (plot on the bottom), for instance, the gray area of DDES is located around $d/h = 0.06$, above the maximum of μ_t/μ. In classical DES97, the gray area would have rather been located at $d/h = 0.015$, inside of the boundary layer, which would have possibly conducted to modeled-stress depletion.

The behavior of DDES shown here is quite satisfactory.

IV. Simulation of Buzz

Figure 10 describes the evolution of the flow during a buzz cycle. To evidence the coherent structures of the flow, the Q criterion [30] has been used

$$Q = -\frac{1}{2}(S_{ij}S_{ij} - \Omega_{ij}\Omega_{ij}) \qquad (6)$$

where S and Ω denote, respectively, the strain and rotation tensor. White surfaces on the figure are isosurfaces of $Q = 8$ and gray surfaces are isosurfaces of Mach number 1 (which allows visualization of the shocks). Black lines are isocontours of Mach number in the symmetry plane of the inlet.

On the first frame, one can see the oblique shocks induced by the ramps (isocontours of Mach number, black lines), as well as the external normal shock. On this frame, the flow remains fully attached. On the second frame, the normal shock is expelled upstream and the separation at its foot appears, at first, not on the compression ramps, but on the sidewalls, and in particular in the corners. Then this separation grows. When the shock reaches the ramp tip, the flow above the ramps and in the inlet section is totally separated (third and fourth frames). Then the separation vanishes, the shock moves downstream (fifth frame), and a supersonic area appears inside the diffuser (sixth frame). Note the occurrence of large-scale hairpin structures over the compression ramps on this frame. The flow then becomes like in supercritical operation (seventh and eighth frames). The internal shock progressively moves upstream (ninth frame) until the flow becomes subcritical again, like in the first frame; a new cycle begins.

Detailed description and analysis of the flow during a buzz cycle, based on the data obtained from this simulation, are given in a subsequent section.

A. Comparison with Experimental Data

1. Pressure Signals and Spectra

Time history of pressure fluctuations corresponding to the location of sensor PS33, located in the diffuser (see Fig. 4) is shown in Fig. 11. The signal from the DDES simulation is compared with the experiment, and to a URANS signal (unsteady Reynolds-averaged Navier–Stokes simulation performed on the same grid).

The calculated signals agree well with the experimental ones, the three main phases that have been previously described (subcritical phase, secondary oscillations, and supercritical phase; see Fig. 4) are visible, the duration of the cycle and the pressure levels are correct. However, the amplitude of the secondary oscillations is too low in the URANS signal, whereas it is correct in the DDES one. The origin of these higher frequencies will be discussed in the following.

The spectra of the pressure records from sensor PS33 (experiment and calculations) during buzz are shown in Fig. 12a. These spectra are obtained with an autoregressive approach based on Burg's method [31]. The levels agree well for the low frequencies.

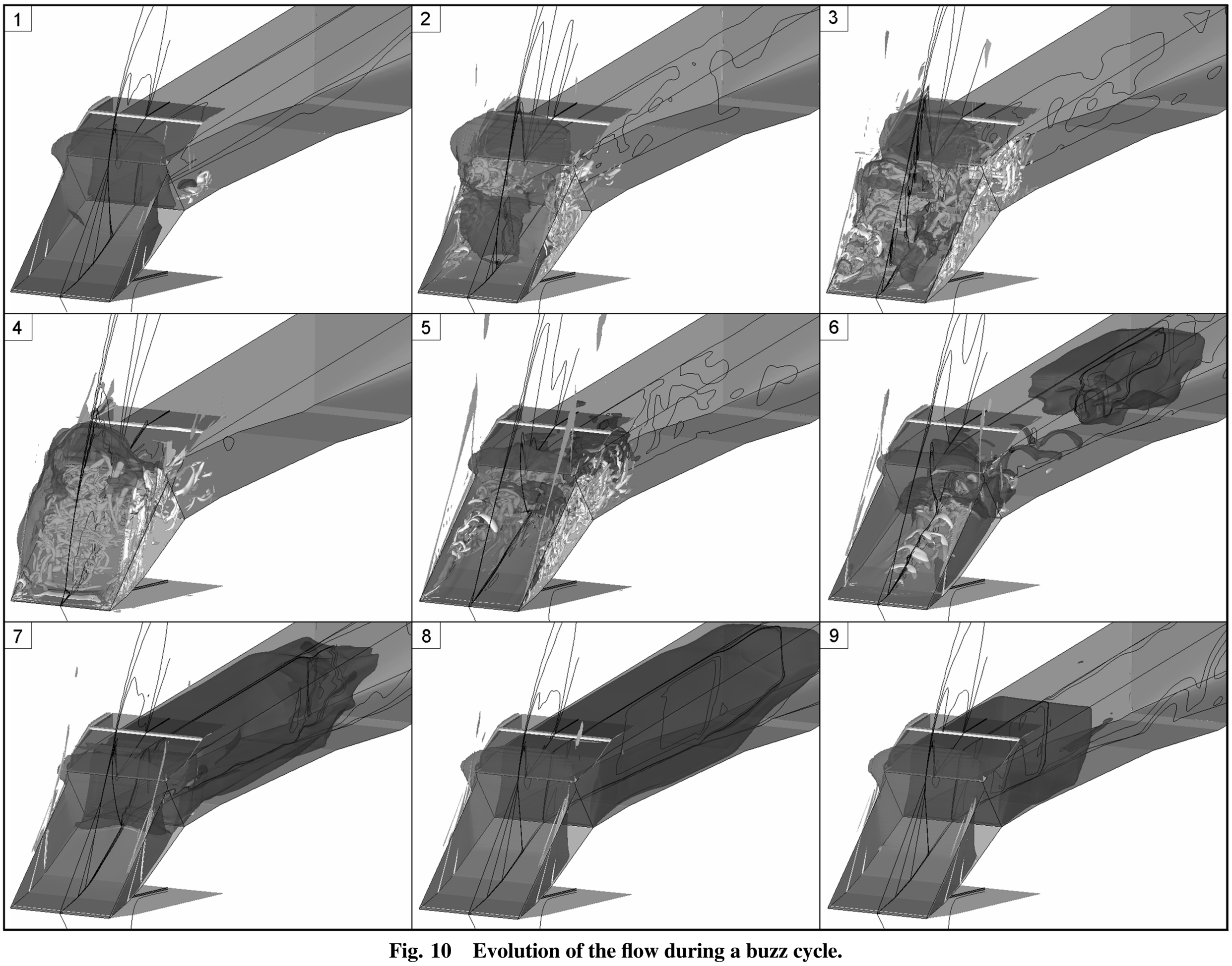

Fig. 10 Evolution of the flow during a buzz cycle.

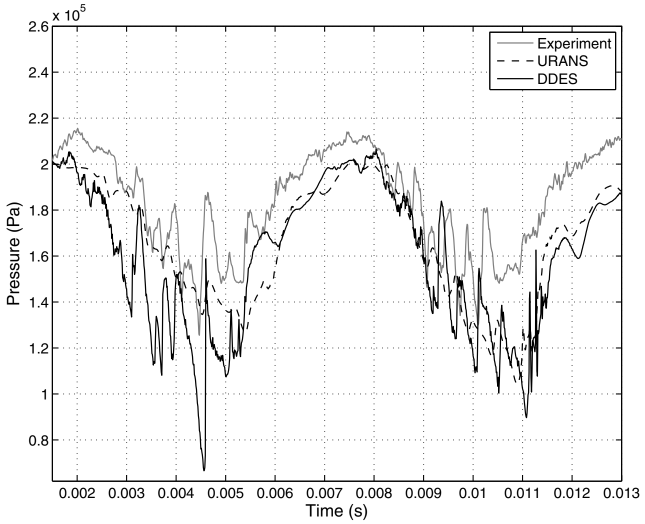

Fig. 11 Comparison of big buzz pressure from experiment, URANS and DDES simulations.

This spectrum displays a peak at 18 Hz (for the experiment, and at 17 Hz for the DDES simulation) which corresponds to the characteristic frequency of buzz. [On the spectra of the records from sensor K18, which is located on the first ramp (Fig. 12b), another important peak appears at 38 Hz. This peak, as well as the next one around 75 Hz, is a harmonic of the main frequency 18 Hz due to the fact that the signal is not sinusoidal.] One can notice that the large-scale self-sustained motion of the shock is well reproduced by both URANS and DDES.

At high frequencies, however, the level of the spectrum from URANS simulation is too low. The level from the DDES one agrees well with the experiment. This difference is even clearer on the spectra of the records from sensor K18. This is due to the fact that high frequencies correspond to turbulence, which is modeled in URANS, whereas it is resolved in DDES. These results indicate that there is a spectral gap between the unsteadiness of the mean field and turbulence at higher frequencies, because only the first one is correctly reproduced by URANS.

2. *Mean and RMS Pressures*

Table 1 shows the calculated and experimentally measured mean pressures and root mean squared (rms) pressures recorded during buzz at sensor K9, which is located in the diffuser.

Table 1 Mean and RMS pressures at sensor K9 (simulation and experiment)

	Mean pressure	RMS pressure
Simulation	1.50×10^5 Pa	3.51×10^4 Pa
Experiment	1.63×10^5 Pa	3.29×10^4 Pa
Error	−7.9%	+6.7%

The calculated mean pressures are lower than the experimental ones, whereas the rms pressures are higher. The probable explanation of this difference is detailed next.

Figure 13 plots the calculated and measured rms pressure profiles during buzz on the lower wall, side wall, and upper wall of the inlet.

These profiles show high values of the rms pressures in the upstream part of the inlet, where the shock motion occurs, in particular over the compression ramps and in the most upstream part of the diffuser. An intermediate zone of relatively low values exists, approximately between the abscissas $x = 0.1$ m and 0.2 m; it corresponds to the zone that always remains subsonic, because it is located between the external shock and the sonic line during the supercritical phases (see Figs. 2d and 2e). More downstream in the diffuser, in the area never reached by the internal shock, the rms pressures are also lower. This evolution of rms pressures along the inlet is correctly reproduced by the simulation. However, the rms pressures are overestimated by the simulation almost everywhere in the inlet. The error remains small in the upstream zone of the inlet; it gets higher in the downstream part of the diffuser.

Because buzz is a periodical phenomenon, the results of the simulation as well as the experimental data can be phase averaged. The procedure consists in dividing each period (i.e., each buzz cycle) into a certain number of phases, then averaging the data over these phases (Fig. 14).

The phase-averaged data allow comparing the pressure levels at different phases of a buzz cycle separately, instead of comparing the global average like in Table 1. The pressure records from the experiment and the simulated flowfields have been averaged on 12 phases (see Fig. 14). Phases 1–5 crudely correspond to the phase of secondary oscillations of the buzz cycle, phases 6 and 7 correspond to the supercritical phase, and phases 8–12 correspond to the subcritical phase (cf. Fig. 4).

Figure 15 shows the phase-averaged pressure fields in the symmetry plane of the inlet, issued from the simulation, during three different phases of a buzz cycle: phase 3 (secondary oscillations), 6 (supercritical), and 10 (subcritical). On this figure, the black lines mark the contour of Mach number $M = 1$, which indicates approximately the average position of normal shocks during each

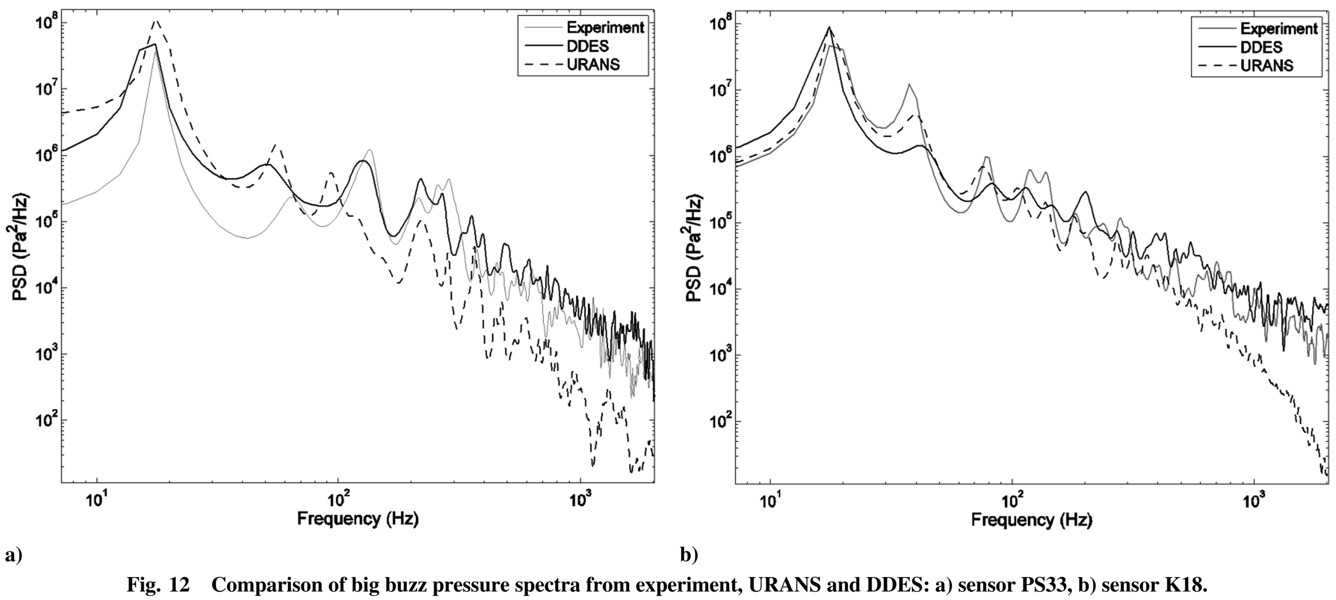

a) b)

Fig. 12 Comparison of big buzz pressure spectra from experiment, URANS and DDES: a) sensor PS33, b) sensor K18.

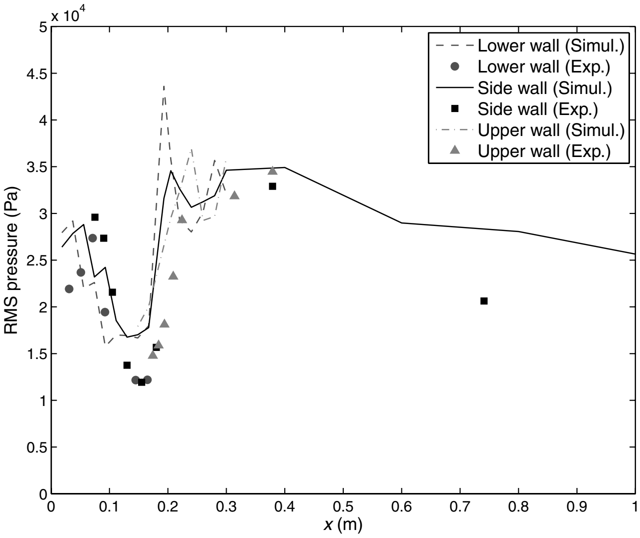

Fig. 13 rms pressures at the walls (simulation and experiment).

phase. The circles on the lower wall indicate the location of the experimental sensors. Figure 16 details the average pressures from simulation and experiment during these three phases, all along the lower wall of the inlet.

It can be noticed that the error on the average pressures changes from one phase to the other. During the supercritical phase, there is almost no error, except for the most downstream sensor. During the subcritical phase, the pressures are underestimated by the simulation in subsonic flow regions. The error is the greatest during the secondary oscillation phase.

These nonnegligible errors on mean pressures as well as on rms pressures can be explained by the following fact: in the experiment, the sonic exit throat is throttled by a butterfly valve, and we do not know precisely its section. Therefore, the section of the sonic throat in the simulation is likely to be different. This has an impact on the mass flow and on the internal pressure, which may explain the difference between the measured and calculated pressures, as well as the slight difference in the buzz frequency that was previously mentioned. Indeed, this frequency is linked to acoustics, and the section of the sonic throat influences the internal Mach number, and so the velocity of the acoustic waves propagation inside the duct.

This hypothesis is confirmed by the following observation: it can be seen from Figs. 15 and 16 that the sensors where the error on pressures is observed are the ones that are located in the most downstream subsonic zone, i.e., the area where the flow is influenced by the exit section. The simulated pressures in the supersonic zones (and in the most upstream subsonic zone, during the supercritical phase), which are not influenced by the exit sonic throat, are very close to the experimental ones.

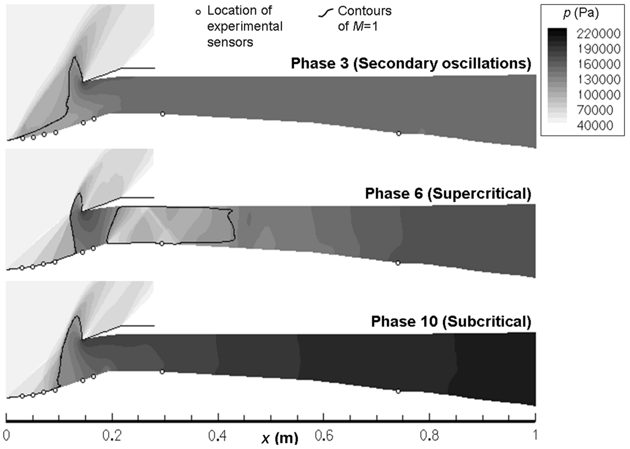

Fig. 15 Simulated phase-averaged pressure fields at different phases of buzz cycle: phases 3 (secondary oscillations), 6 (supercritical), and 10 (subcritical).

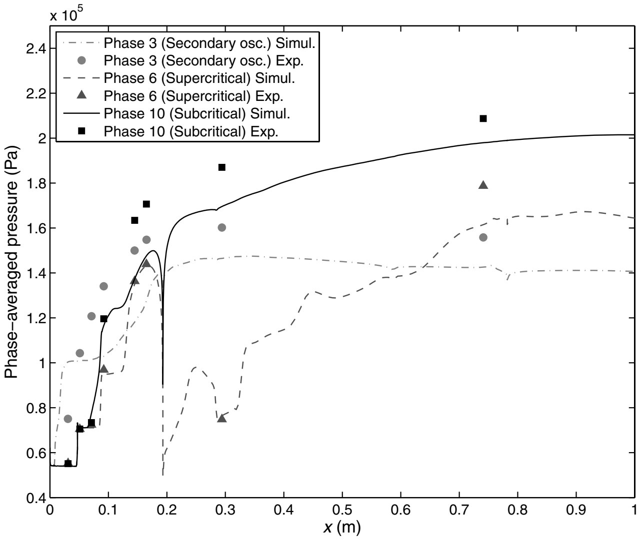

Fig. 16 Phase-averaged pressures (simulation and experiment) at the lower wall at the same phases as in Fig. 15.

3. *Wavelet Transforms*

Spectra such as the ones shown in Fig. 12 allow comparing the global frequency content of the different signals. However, it can be seen on the signals (Fig. 11) that this content is not constant, but changes with time. The spectra based on the Fourier transform do not take this evolution into account. This is why an accurate comparison should be done using time-frequency representations, which plot the

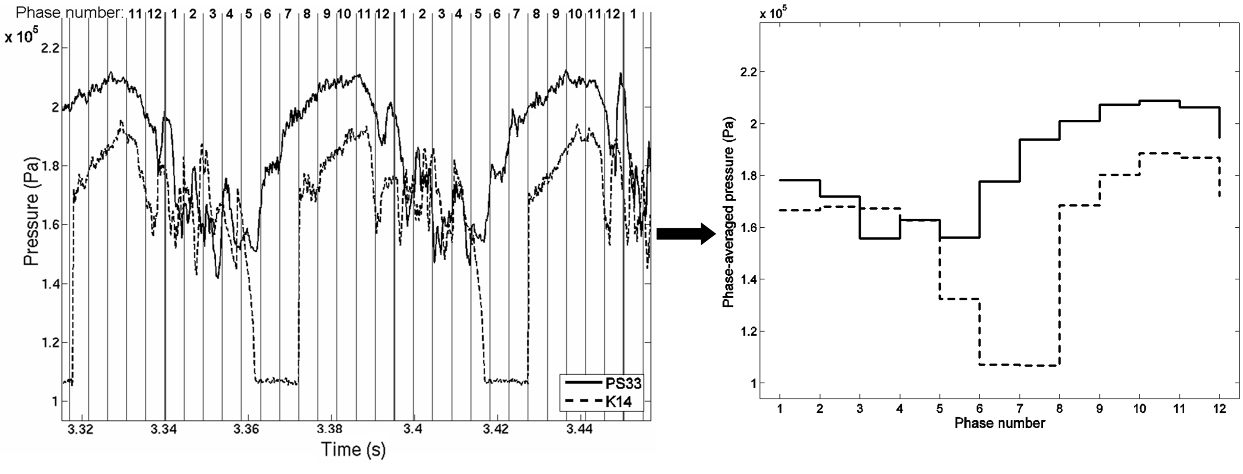

Fig. 14 Procedure to compute phase average: each period is divided into 12 phases over which the data is averaged.

energy content of the signal against time and frequency. Among the family of time-frequency methods, the wavelet transform has proven to be efficient in investigating the buzz phenomenon [15].

A wavelet is a function $\psi(t)$ with zero mean and finite energy. We are using here the so-called Gabor wavelet, defined as

$$\psi(t) = \frac{1}{\sqrt{2\pi\sigma^2}} e^{-t^2/2\sigma^2} e^{-2i\pi\eta t} \tag{7}$$

where σ and η are two parameters allowing one to control, respectively, the time dispersion and the frequency of the wavelet.

The wavelet transform $Wx(\tau, s)$ of a signal $x(t)$ is defined as

$$Wx(\tau, s) = \int_{-\infty}^{+\infty} x(t) \frac{1}{\sqrt{s}} \psi^* \left(\frac{t - \tau}{s} \right) \mathrm{d}t \tag{8}$$

The asterisk (*) stands for the complex conjugate; s is a scale factor, which can be linked to a frequency $f = \eta / s$; Wx is complex. The plot of its squared modulus $|Wx(\tau, f)|^2$, called scalogram, is a time-frequency representation of the signal $x(t)$. It represents an energy density (its unit is $\mathrm{Pa}^2 \cdot \mathrm{Hz}^{-1} \cdot \mathrm{s}^{-1}$).

The reader interested in the theoretical aspects of this method can refer to [32–34].

Figure 17 shows the time-frequency representation (or scalograms) of DDES (left) and experimental (right) signals, obtained by wavelet transform. The wavelet parameters $\sigma = 0.1$ and $\eta = 15$ have been retained here, for they provide a good compromise between time and frequency resolutions [15].

The two plots of Fig. 17 have the same appearance. On both plots, the buzz frequency is clearly visible as a regular, thin, horizontal line at 18 Hz. The secondary oscillations also appear under the form of “spots” at higher frequencies, which are regularly distributed in time. It can be seen that the frequency of these oscillations is variable from one cycle to another, and so is their amplitude. They even almost do not exist during certain cycles (the third simulated cycle and the fifth experimental cycle, for instance).

The main differences between DDES and the experiment are the buzz oscillations amplitude, which is higher in the DDES signal, and the secondary oscillations frequency, which is in general lower in the DDES signal.

Finally, the comparison between experimental and simulated data shows a difference between the levels of mean pressures and rms pressures, which can be explained by a probable difference in the exit sonic throat section. However, a detailed analysis of the experimental and simulated results show that all physical phenomena that were experimentally observed are present and correctly reproduced by the simulation. A physical analysis of buzz, based on the data issued from the numerical simulation, is therefore possible.

B. Study of the Shear Layer

An important feature of the flow during the subcritical phase and the secondary oscillations is a shear layer located over the ramps. This shear layer develops between the separated area appearing on the ramps during these phases and the high-speed flow passing over it. It plays in particular a major role in the mechanism of the secondary oscillations, as will be explained in the next section. Figure 18a shows this shear layer (numerical Schlieren picture), and Fig. 18b shows the corresponding velocity profiles at different abscissas.

The vorticity thickness of a shear layer is defined as:

$$\delta_\omega = \frac{U_+ - U_-}{\max\limits_{[y]}(\partial U / \partial y)} \tag{9}$$

where U_+ and U_- are the upper and lower velocities (respectively, upon and below the shear layer).

For the four profiles of Fig. 18, this definition gives the following: $\delta_\omega = 3$, 3, 6, and 12 mm.

The following semi-empirical formula [35] allows one to crudely estimate the frequency range of the Kelvin–Helmoltz instability:

$$f_{K-H} \approx 0.135 \frac{U_+ - U_-}{\delta_\omega} \tag{10}$$

For the first profile of Fig. 18 ($x = 0.03$), one obtains

$$f_{K-H} = 15{,}900 \text{ Hz}$$

Figure 19 shows the spectrum of the simulated pressure signal issued from sensor K18 located on the compression ramp, during the phase in which the shear layer exists. It shows a wide peak around

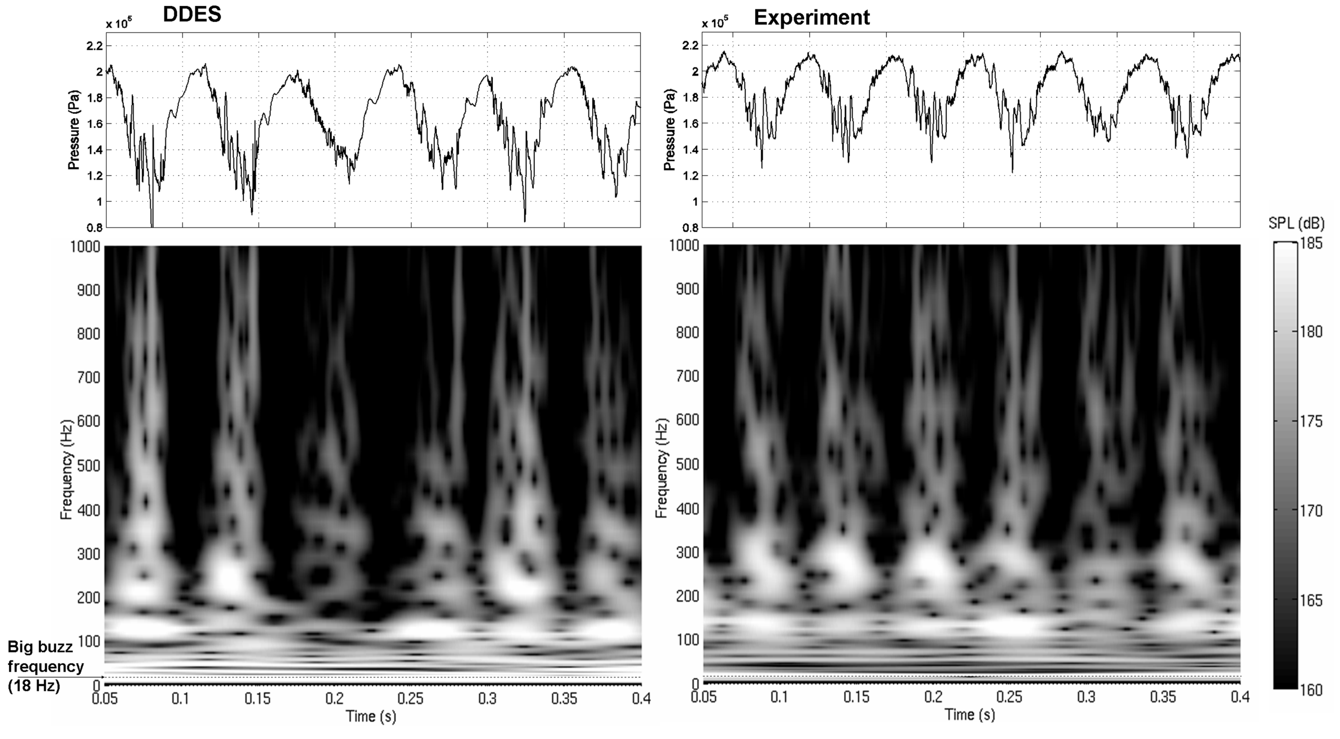

Fig. 17 Wavelet transform of pressure signals from DDES and experiment.

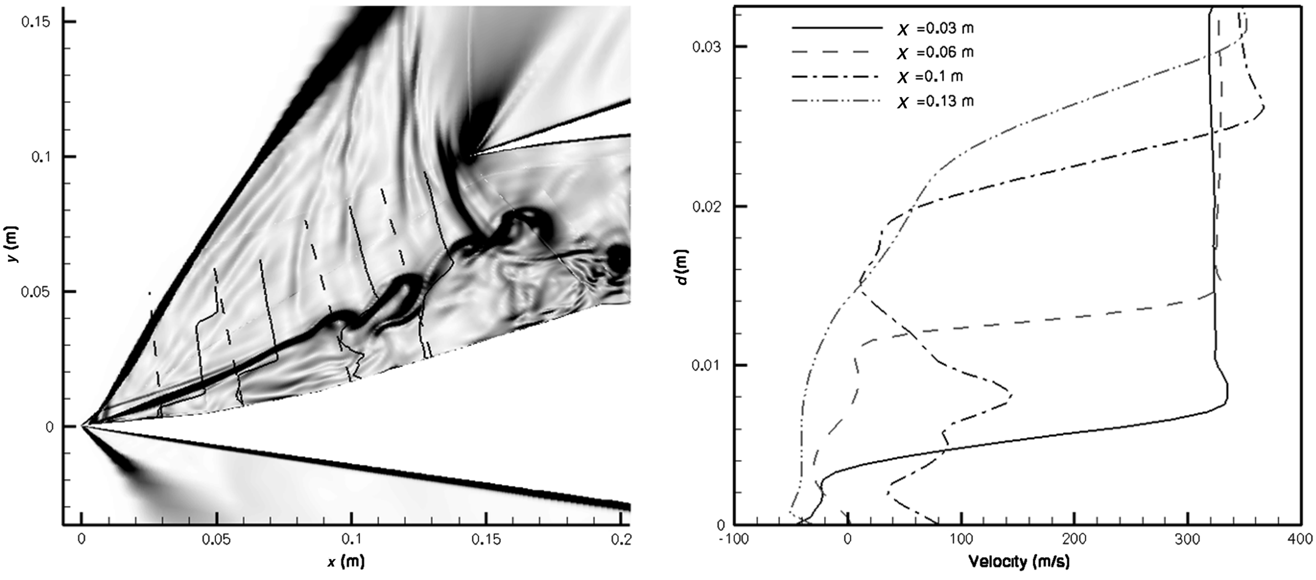

a) b)

Fig. 18 Velocity profiles over the compression ramps at $t = 0.0755$ s.

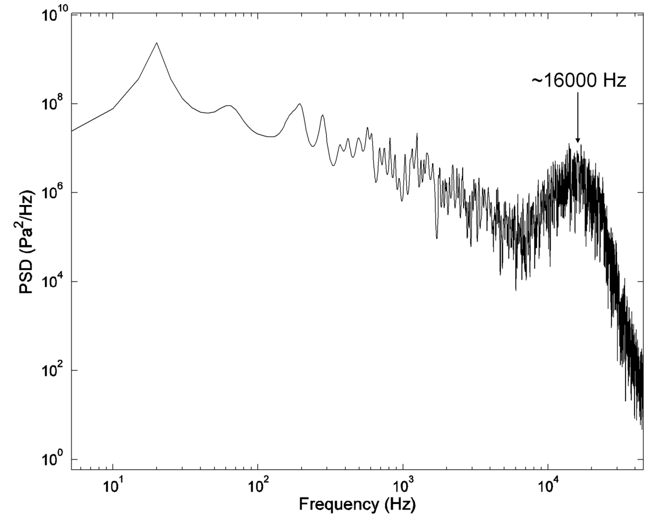

Fig. 19 Spectrum of the simulated pressure signal at sensor K18 (first ramp).

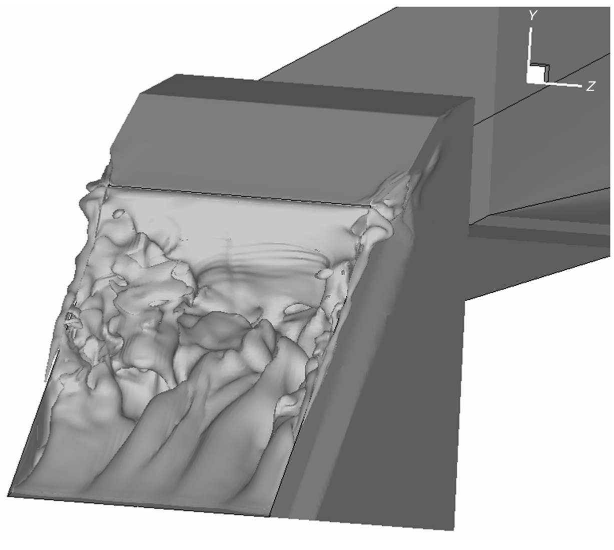

Fig. 20 Spanwise undulations of the shear layer.

16 KHz, which indicates the existence of Kelvin–Helmoltz instability in the shear layer, in this area.

It has also to be noticed that this shear layer is not two-dimensional but shows undulations in the spanwise direction, as can be seen in Fig. 20. In this figure, the shear layer is materialized by the isosurface of velocity 170 m/s.

C. Description of Buzz Flow and Physical Analysis

We now get interested in one particular simulated buzz cycle, which will be described in detail.

Visualization such as the one plotted in Fig. 21 gives a general vision of the evolution of the flow in the whole inlet during a buzz cycle. It plots the static pressure p, taken at the central line of the inlet (indicated by the dotted line, in the sketch of the inlet on the top of the

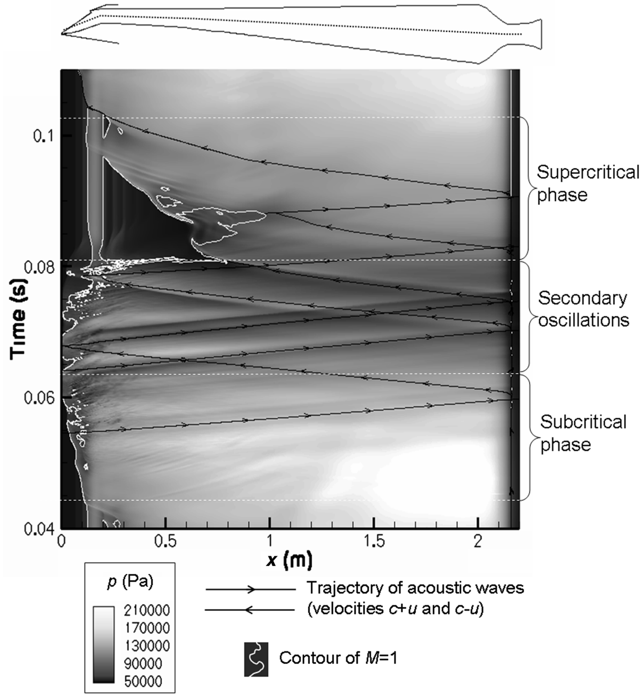

Fig. 21 Contour of pressure against space and time, during a buzz cycle.

figure), against space (the abscissa x, horizontal axis), and time (vertical axis).

This plot allows one to see most of the flow features:

1) The trajectory of the normal shocks, which are materialized on the figure by the contour of $M = 1$ (white line). This contour also shows the location of the sonic throat.

2) The acoustic waves moving through the duct, and reflecting on the sonic throat. In this drawing, the lines with arrowheads represent the trajectory of acoustic waves moving downstream and upstream, respectively, with velocities $c + u$ and $c - u$ (where c is the local speed of sound).

3) The separated and turbulent flow on the compression ramps also appears, approximately from $t = 0.05$ to $t = 0.08$ s.

The three phases of the buzz cycle already described in Fig. 4 (subcritical phase, secondary oscillations, and supercritical phase) are also visible on these plots.

In the following, we will successively describe the development of these three phases. Figure 22 shows the calculated flow (Schlieren pictures and streamlines) at each time t mentioned in this description.

1. *Subcritical Phase*

At time $t = 0.045$ s, the normal shock is on the compression ramps and is pushed upstream by a high internal pressure. At $t = 0.054$ s, it reaches the first compression ramp. Because the flow over this ramp has crossed only one oblique shock, its Mach number is higher than over the second ramp, and the normal shock gets stronger. A separated area begins to develop at its foot.

At $t = 0.0585$ s, the separated area has grown; the normal shock is replaced by an oblique shock, which is generated by this separated area. The flow just behind it is supersonic; it becomes subsonic while passing through a series of shocklets. Between this high-velocity

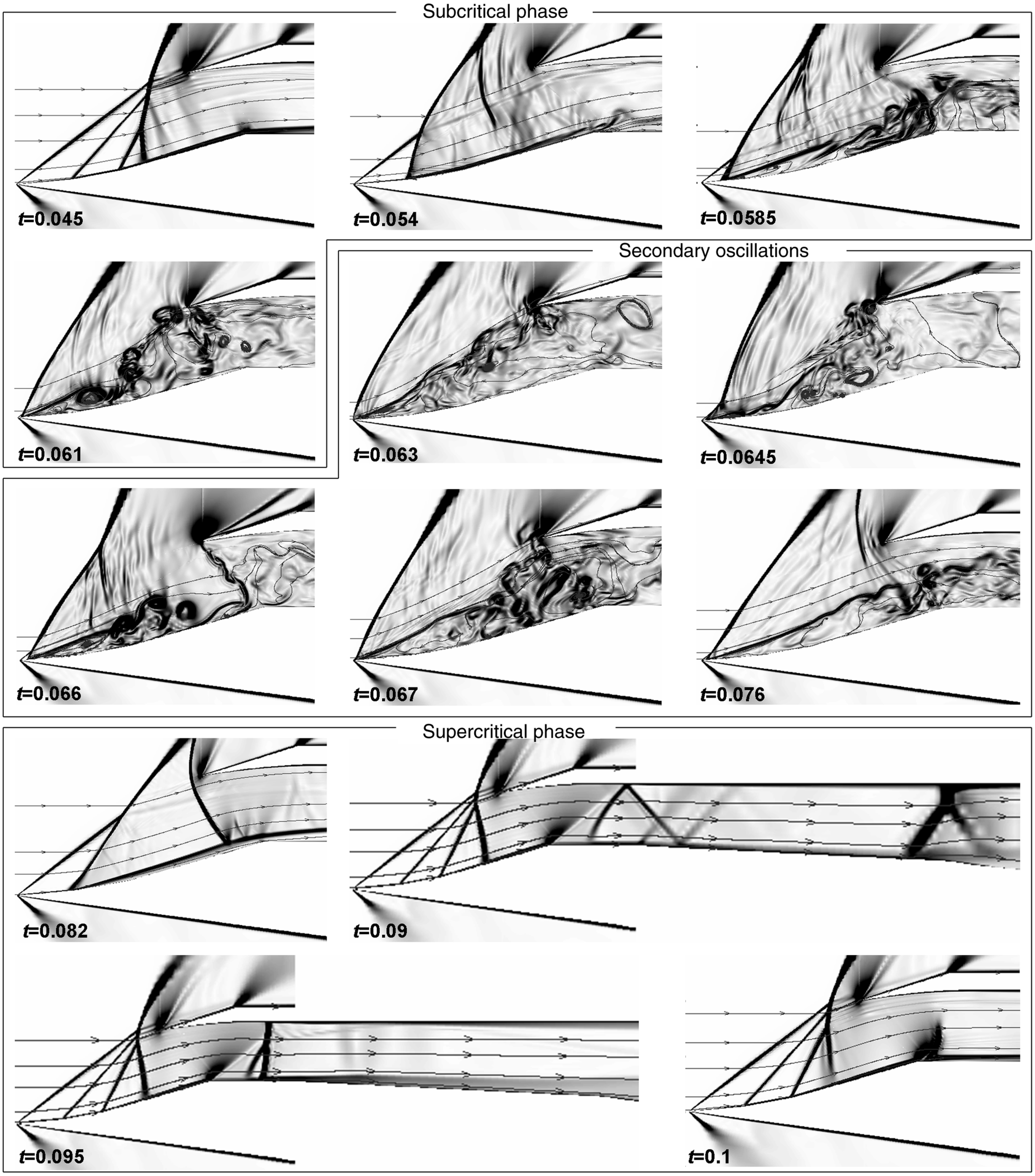

Fig. 22 Numerical Schlieren pictures and streamlines during a big buzz cycle.

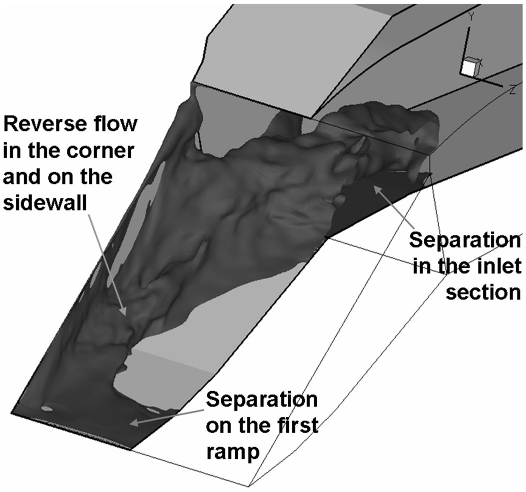

Fig. 23 Isosurface of phase-averaged velocity $u = -1$ m/s during subcritical phase, in one half of the inlet.

flow and the low-velocity flow that exists in the separated area, a shear layer appears. At the same time, the inlet section of the diffuser is widely obstructed by the separated flow.

Figure 23 shows the boundary of the separated flow area during this phase (isosurface of the phase-averaged velocity $u = -1$ m/s during phase 10, see Fig. 14). It shows that the two separated areas, i.e., the one at the shock foot and the one in the diffuser, are in fact one; although the flow is partially attached on the compression ramps, it is fully separated in the corners and on the sidewalls. The reverse flow in this area feeds the separation on the first ramp; that is the reason why this latter separated area is growing during this phase.

Around $t = 0.061$ s, the shock reaches the ramp tip. Kelvin–Helmotz instability develops in the shear layer (see details in the previous section). The two separated areas have merged and they obstruct almost entirely the inlet section. The entering mass flow is almost zero and, behind this obstruction, the pressure falls. This low-pressure zone is then propagated downstream in the diffuser by an expansion wave which is visible in Figs. 21 and 24 (it is indicated by a dotted line on the latter). This marks the beginning of the secondary oscillations.

2. *Secondary Oscillations*

The secondary oscillations occur approximately between $t = 0.063$ and $t = 0.078$ s. Their frequency (which is not exactly constant) is around 200 Hz. They cause a shock motion which is visible in Fig. 21 (white line). Acoustic waves propagating in the diffuser, which are also visible in Fig. 21, are emitted during this phase.

Figure 24 shows the plot of *u* against space and time, taken from a line located close to the lower wall (dotted line), during the secondary oscillations phase.

The dark areas indicate a reverse flow ($u < 0$). It can be seen on this figure that, during the oscillations, the flow on the ramps was most of the time separated, but periodically reattached. These attached zones (which appear in light gray on Fig. 24) were then carried downstream at the flow velocity (which is materialized by the white lines with arrowheads).

The mechanism of these oscillations (summed up by the sketch in Fig. 25) is as follows:

From $t = 0.061$ s to 0.063 s, the separated area is still growing, fed by the reverse flow from the diffuser. It pushes upstream and straightens up the shock, which gets detached at a very short distance, around 0.1 mm, upstream the ramp tip (Fig. 25a). The incident flow on the ramps is now horizontal and subsonic, and so there is no shock and no separation generated on them. The separated area which existed on the ramps is convected downstream, and it is replaced by an attached flow. Then, because there is no separated area on the ramps, the shock moves downstream again. The total time during which it remains detached is around 3.10^{-4} s.

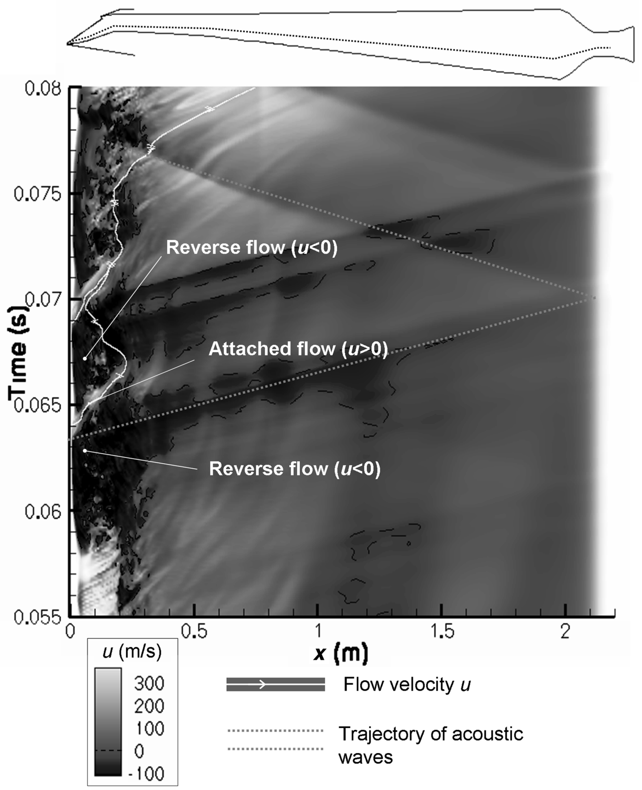

Fig. 24 Plot of *u* against space and time, during secondary oscillations.

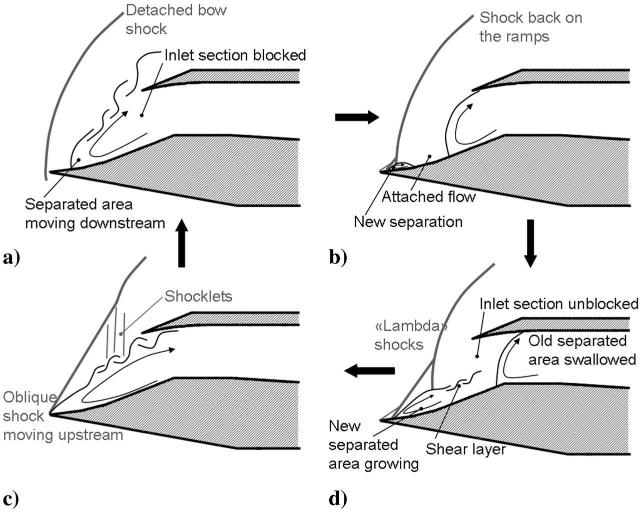

Fig. 25 Mechanism of the secondary oscillations.

At $t = 0.0645$ s, the shock is back on the ramps, and a new separation begins to develop at its foot (Fig. 25b). At $t = 0.066$ s, it has given birth to a new separated area on the ramps, with a "lambda" shock interaction, and a new shear layer (Fig. 25c). At the same time, the old separated area is swallowed by the inlet, which is not obstructed any more. The incoming mass flow increases, and so does the pressure in the diffuser. This high-pressure zone is propagated downstream in the diffuser by a compression wave (visible in Fig. 21). The new separated area continues to grow until it occupies all compression ramps ($t = 0.067$ s, Fig. 25d). The oblique shock, which was formerly the upstream branch of the lambda, moves upstream to the ramp tip. The situation is identical to the one observed at $t = 0.0645$ s. A new cycle of secondary oscillations begins.

Actually, the mechanism of these oscillations is very close to the pulsations observed on unsteady spiked body flows [36–38]. The ramps would play the role of the spike, and the body would be the obstructed inlet section.

A second cycle takes place between $t = 0.067$ and 0.0725 s, during which another expansion wave and another compression wave are emitted. At $t = 0.076$ s, while a third cycle is taking place, the expansion wave which was emitted at $t = 0.06$ s and was reflected on the sonic throat (see Figs. 21 and 24) comes back to the inlet section. The downstream pressure falls, and the separation in the inlet disappears. The normal shock starts moving downstream. At $t = 0.082$ s, it passes on the second compression ramp. There is no more separation at its foot. At the same time, a supersonic zone and an internal shock appear inside the diffuser. The inlet is in supercritical operation.

3. *Supercritical Phase*

The internal shock reaches its most downstream position, around $x = 0.8$ m, almost immediately. Then it is pushed upstream by pressure waves coming from downstream. These waves are issued from the reflection of the compression waves emitted during the secondary oscillations on the sonic throat (see Fig. 21). At $t = 0.09$ s, the shock is at $x = 0.4$ m. Inside the duct, between the inlet section and the shock, the flow is supersonic and fully attached. The URANS and DDES simulations give identical results during this phase. The inlet mass flow is high.

As the internal pressure increases, the shock moves upstream ($t = 0.95$ s) until it gets expelled and merges with the external normal shock. The latter is then pushed and starts to move upstream ($t = 0.1$ s). The flow is subcritical again. A new buzz cycle begins.

V. Conclusions

A DDES (delayed detached-eddy simulation) of supersonic inlet buzz at Mach number 1.8 has been conducted on a 20 million points grid. It has been compared with experimental data (pressure records and Schlieren visualizations) obtained during wind-tunnel tests on a mixed-compression, rectangular inlet model. At this Mach number, the experimental data indicated that the buzz was linked to a separation on the compression ramps (Dailey criterion).

The DDES approach gives very satisfactory results. The comparison shows a good agreement between experimental and calculated results. All features of buzz flow that had been experimentally observed are present and well reproduced in the simulation: the motion of the normal shock, the large separation that appears on the compression ramps and obstructs the inlet, the secondary oscillations of pressure that occur when the normal shock reaches the ramp tip.

The simulation provided a large amount of information about the inlet flow and its evolution during buzz, in particular about parts of the flow which were not accessible to experimental measures. This data allowed a detailed description and physical analysis of buzz flow. It has been observed in particular that the separation does not appear on the compression ramps, but rather in the corners and on the sidewalls. A description and an explanation of the mechanism at the origin of the secondary oscillations have been proposed.

DDES appears to be an appropriate approach for the study of complex flows, possibly on industrial configurations, with separated regions whose location is not fixed by the geometry. Further analysis is to be carried on. The ability of the numerical simulation to accurately predict the buzz onset, and in particular the value of the captured mass flow when buzz starts, still has to be evaluated.

References

[1] Oswatitsch, K., *Der Druckrückgewinn bei Geschossen mit Rückstossantrieb bei hohen Übershallgeschwindigkeiten*, Der Wirkungsgrad vos Stossdiffusoren, Rept. No. 1005 Forsch. und Entwickl. des Heereswaffenamtes, Göttingen, Germany, 1944.

[2] Ferri, A., and Nucci, L. M., "The Origin of Aerodynamic Instability of Supersonic Inlets at Subcritical Conditions," NACA RM L50K30, 1951.

[3] Dailey, C. L., "Supersonic Diffuser Instability," Ph.D. Thesis, California Inst. of Technology, Pasadena, CA, 1954.

[4] Trimpi, R., "A Theory for Stability and Buzz Pulsation Amplitude in Ram Jets and an Experimental Investigation Including Scale Effects," NACA Rept. 1265, 1956.

[5] Fisher, S. A., Neale, M. C., and Brooks, A. J., "On the Sub-Critical Stability of Variable Ramp Intakes at Mach Numbers Around Two," National Gas Turbine Establishment, England, Rept. No. ARC-R/M-3711, Feb. 1970.

[6] Nagashima, T., Obokata, T., and Asanuma, T., "Experiment of Supersonic Air Intake Buzz," Institute of Space and Aeronautical Science, Tokyo, Rept. No. 481; *Space Aeronautics Research and Development Mechanism*, Vol. 37, No. 7, Nov. 1972, pp. 165–209.

[7] Hongprapas, S., Kozak, J. D., Moses, B., and Ng, W. F., "A Small Scale Experiment for Investigating the Stability of a Supersonic Inlet," AIAA Paper 97-0611, Jan. 1997.

[8] Sterbentz, W., and Evvard, J., "Criterions for Prediction and Control of Ram-Jet Flow Pulsations," NACA RM E51C27, 1951.

[9] Leynaert, J., "Une description globale élémentaire du pompage des prises d'air supersoniques," ONERA TN 47/2149 A, 1968.

[10] Leynaert, J., "Pompage dans les entrées d'air supersoniques," *L'Aéronautique et l'Astronautique*, Vol. 22, 1970, pp. 47–62.

[11] Newsome, R. W., "Numerical Simulation of Near-Critical and Unsteady, Subcritical Inlet Flow," *AIAA Journal*, Vol. 22, No. 10, 1984, pp. 1375–1379.

[12] Lu, P. J., and Jain, L. T., "Numerical Investigation of Inlet Buzz Flow," *Journal of Propulsion and Power*, Vol. 14, No. 1, 1998, pp. 90–100.

[13] Fujiwara, H., Murakami, A., and Watanabe, Y., "Numerical Analysis on Shock Oscillation of Two-Dimensional External Compression Inlets," AIAA Paper 2002-2740, June 2002.

[14] Trapier, S., Duveau, P., and Deck, S., "Experimental Study of Supersonic Inlet Buzz," *AIAA Journal*, Vol. 44, No. 10, 2006, pp. 2354–2365.
doi:10.2514/1.20451

[15] Trapier, S., Deck, S., Duveau, P., and Sagaut, P., "Time-Frequency Analysis and Detection of Supersonic Inlet Buzz," *AIAA Journal*, Vol. 45, No. 9, 2007, pp. 2273–2284.

[16] Spalart, P. R., Deck, S., Shur, M. L., Squires, K. D., Strelets, M., and Travin, A., "A New Version of DES, Resistant to Ambiguouis Grid Densities," *Theoretical and Computational Fluid Dynamics*, Vol. 20, 2006, pp. 181–195.
doi:10.1007/s00162-006-0015-0

[17] Péchier, M., Guillen, Ph., and Caysac, R., "Magnus Effect over Finned Projectiles," *Journal of Spacecraft and Rockets*, Vol. 38, No. 4, 2001, pp. 542–549.

[18] Deck, S., Duveau, P., d'Espiney, P., and Guillen, P., "Development and Application of Spalart Allmaras One Equation Turbulence Model to Three-Dimensional Supersonic Complex Configurations," *Aerospace Science and Technology*, Vol. 6, No. 3, 2002, pp. 171–183.
doi:10.1016/S1270-9638(02)01148-3

[19] Raverdy, B., Mary, I., Sagaut, P., and Liamis, N., "High-Resolution Large-Eddy Simulation of Flow Around Low Pressure Turbine Blade," *AIAA Journal*, Vol. 41, No. 3, 2003, pp. 390–397.

[20] Larchevêque, L., Labbé, O., Mary, I., and Sagaut, P., "LES of a Compressible Flow past a Deep Cavity," *Physics of Fluids*, Vol. 15, No. 1, 2003, pp. 193–210.
doi:10.1063/1.1522379

[21] Deck, S., "Numerical Simulation of Transonic Buffet over a Supercritical Airfoil," *AIAA Journal*, Vol. 43, No. 7, July 2005, pp. 1556–1566.

[22] Deck, S., and Thorigny, P., "Unsteadiness of an Axisymmetric Separating-Reattaching Flow: Numerical Investigation," *Physics of Fluids* Vol. 19, No. 6, 2007, p. 065103.
doi:10.1063/1.2734996.

[23] Dandois, J., Garnier, E., and Sagaut, P., "Unsteadiness Numerical Simulation of Active Separation Control by a Synthetic Jet," *Journal of Fluid Mechanics*, Vol. 574, 2007, pp. 25–58.
doi:10.1017/S0022112006003995

[24] Simon, F., Deck, S., Guillen, P., and Sagaut, P., "Unsteadiness Reynolds-Averaged Navier-Stokes/Large-Eddy Simulations of Supersonic Base Flow," *AIAA Journal*, Vol. 44, No. 11, Nov. 2006, pp. 2578–2590.
doi:10.2514/1.21366

[25] Spalart, P. R., Jou, W.-H., Strelets, M., and Allmaras, S. R., "Comments on the Feasibility of LES for Wings, and on a Hybrid RANS/LES Approach," *In Proceedings, 1st AFSOR International Conference on DNS/LES*, Greyden Press, Columbus, OH, 1997, pp. 137–147.

[26] Menter, F. R., Kuntz, M., and Bender, R., "A Scale-Adaptative Simulation Model for Turbulent Flow Predictions," AIAA Paper 2003-0767, 2003.

[27] Sagaut, P., Deck, S., and Terracol, M., *Multiscale and Multiresolution Approaches in Turbulence*, Imperial College Press, London, 2006.

[28] Deck, S., "Zonal Detached-Eddy Simulation of the Flow Around a High-Lift Configuration," *AIAA Journal*, Vol. 43, No. 11, Nov. 2005, pp. 2372–2384.

[29] Spalart, P. R., "Young-Person's Guide to Detached-Eddy Simulation Grids," NASA TR CR-2001-211032, July 2001.

[30] Jeong, J., and Hussain, F., "On the Identification of a Vortex," *Journal of Fluid Mechanics*, Vol. 285, Feb. 1995, pp. 69–94. doi:10.1017/S0022112095000462

[31] Burg, J. P., "Maximum Entropy Spectral Analysis," *Modern Spectrum Analysis*, edited by D. G. Childers, IEEE Press, New York, 1978, pp. 34–41.

[32] Flandrin, P., *Temps-fréquence*, Editions Hermès, Paris, 1993.

[33] Mallat, S., *A Wavelet Tour of Signal Processing*, Academic Press, New York, 1999.

[34] Farge, M., "Wavelet Transforms and Their Applications to Turbulence," *Annual Review of Fluid Mechanics*, Vol. 24, 1992, pp. 395–457. doi:10.1146/annurev.fl.24.010192.002143

[35] Huerre, P., and Rossi, M., "Hydrodynamic Instabilities in Open Flows," *Hydrodynamics and Nonlinear Instabilities*, edited by C. Godrèche and P. Manneville, Cambridge Univ. Press, Cambridge, England, U.K., 1998, pp. 81–214.

[36] Feszty, D., Badcock, K. J., and Richards, B. E., "Driving Mechanisms of High-Speed Unsteady Spiked Body Flows, Part 1: Pulsation Mode," *AIAA Journal*, Vol. 42, No. 1, Jan. 2004, pp. 95–106.

[37] Maull, D. J., "Hypersonic Flow over Axially Symmetric Spiked Bodies," *Journal of Fluid Mechanics*, Vol. 8, 1960, pp. 584–592. doi:10.1017/S0022112060000815

[38] Mair, W., "Experiments on Separation of Boundary Layer on Probes in Front of Blunt Nosed Bodies in a Supersonic Stream," *Philosophical Magazine*, Vol. 43, No. 342, July 1952, pp. 593–601.

R. So
Associate Editor